Draft version April 21, 2017
Preprint typeset using LaTeX style emulateapj v. 01/23/15

arXiv:1704.05878v1 [astro-ph.EP] 19 Apr 2017

NIR-DRIVEN MOIST UPPER ATMOSPHERES OF SYNCHRONOUSLY ROTATING TEMPERATE TERRESTRIAL EXOPLANETS

Yuka Fujii
NASA Goddard Institute for Space Studies, 2880 Broadway, New York, NY and
Earth-Life Science Institute, Tokyo Institute of Technology, Ookayama, Meguro, Tokyo 152-8550, Japan

Anthony D. Del Genio
NASA Goddard Institute for Space Studies, 2880 Broadway, New York, NY

David S. Amundsen
NASA Goddard Institute for Space Studies, 2880 Broadway, New York, NY and
Department of Applied Physics and Applied Mathematics, Columbia University, New York, NY 10025, USA

Draft version April 21, 2017

ABSTRACT

H_2O is a key molecule in characterizing atmospheres of temperate terrestrial planets, and observations of transmission spectra are expected to play a primary role in detecting its signatures in the near future. Detectability of H_2O absorption features in transmission spectra depends on the abundance of water vapor in the upper part of the atmosphere. While the stratospheric water vapor mixing ratio of the Earth is less than 10^{-5} due to the cold trap, the efficiency of the cold trap depends on atmospheric properties. Here we study the three-dimensional distribution of atmospheric H_2O for synchronously rotating Earth-sized aquaplanets using the general circulation model (GCM) ROCKE-3D, and examine the effects of total incident flux and stellar spectral type. We observe a more gentle increase of the water vapor mixing ratio in response to increased incident flux than one-dimensional models suggest, in qualitative agreement with the climate-stabilizing effect of clouds around the substellar point previously observed in GCMs applied to synchronously rotating planets. However, the water vapor mixing ratio in the upper atmosphere starts to increase while the surface temperature is still moderate. This is explained by the circulation in the upper atmosphere, which is seen in the runs with high incident flux, causing efficient vertical transport of water vapor. This circulation is driven by the radiative heating due to absorption by water vapor and cloud particles in the upper atmosphere. The interplay between this vertical transport of water vapor and the radiative heating may play the key role in determining the steady state of the water vapor profile. Consistently, the water vapor mixing ratio is found to be well correlated with the near-infrared portion of the incident flux. Our results imply that various levels of water vapor mixing ratio in the upper atmosphere may be expected for synchronously rotating temperate terrestrial planets, and that for the more highly irradiated ones the H_2O absorption features in the transmission spectra are strengthened by a factor of a few, loosening the observational demands for a direct H_2O detection.

Subject headings: planets and satellites: atmospheres, planets and satellites: terrestrial planets

1. INTRODUCTION

One of the primary interests in future observations of Earth-sized planets is the presence of H_2O, both as a tracer of habitable conditions and as a clue to the origin and evolutional pathways of the planets. Its spectral signatures may be targeted in the near future through transmission spectroscopy using JWST or next-generation ground-based telescopes. Although H_2O signatures have been detected in the atmospheres of hot Jupiters (e.g. Tinetti et al. 2007; Sing et al. 2016), detecting molecular signatures, including H_2O, on temperate terrestrial planets is exceedingly challenging (Cowan et al. 2015) because of the small planetary radius and the small scale height (due to the lower temperature and presumably larger mean molecular weight). Besides, while H_2O is a dominant opacity source of Earth's atmosphere, its signatures in the transmission spectra of temperate planets are not strong due to the "cold trap", i.e., water vapor evaporated from the surface is transported upward, but condenses as air rises and cools, and most of it precipitates, leaving the stratosphere—where transmission spectroscopy typically probes—fairly dry. Several studies modeling transmission spectra of the Earth found modest signatures of water vapor (e.g. Ehrenreich et al. 2006; Kaltenegger & Traub 2009; Bétrémieux & Kaltenegger 2013; Misra et al. 2014). However, the efficiency of the cold trap depends on the atmospheric properties in general. Thus, modeling the water vapor mixing ratio profiles is an issue of interest in the context of evaluating the observability of atmospheric signatures of transiting terrestrial planets.

The mixing ratio of water vapor in the stratosphere is also closely related to planetary water loss and thus planetary habitability. Kasting et al. (1993) considered the maximum stratospheric water vapor mixing ratio that would allow for a planet to sustain an amount of water equivalent to the Earth's oceans over the Earth's age, $\sim 3 \times 10^{-3}$, as a criterion for the inner edge of the habit-

able zone (the threshold for the moist-greenhouse stage). Motivated mainly by this "habitability" aspect, atmospheric models with different levels of complexity have examined stratospheric water vapor, or equivalently, the efficiency of the cold trap, with varying planetary properties.

Kasting et al. (1993) and Kopparapu et al. (2013) used a simple one-dimensional (1D) model with a saturated troposphere and an isothermal stratosphere to examine the response of the stratospheric water vapor mixing ratio to increased instellation. They found a transition from an Earth-like dry upper atmosphere to a water-dominated atmosphere, driven by the increase of the surface temperature. The above-mentioned critical mixing ratio ($\sim 3 \times 10^{-3}$) is reached when the surface temperature is ~340 K. Kodama et al. (2015) also showed a similarly rapid transition to a water-dominated atmosphere as a function of incident flux using a 1D radiative-convective model.

Wordsworth & Pierrehumbert (2013, 2014) argued that the degree to which a condensible gas is transported from the surface is represented by $\mathcal{M} = m_v p_v L / m_n p_n c_p T$ where L, c_p, and T are the specific latent heat of the condensing gas, the specific heat capacity at constant pressure of the non-condensing gas, and surface temperature, respectively, while $m_{\{v,n\}}$ and $p_{\{v,n\}}$ are molar masses and the partial pressures of the condensing (v) or non-condensing (n) gases. A moist upper atmosphere occurs when $\mathcal{M} > 1$. This indicates that the efficiency of the transport from the surface depends on the atmospheric composition, in particular the abundance of non-condensing gases, in addition to incident flux (Wordsworth & Pierrehumbert 2014). Wordsworth & Pierrehumbert (2013) used 1D radiative-convective models with different levels of CO_2 and incident flux, and identified the range of parameters that leads to an inefficient cold trap.

Rauer et al. (2011) and Rugheimer et al. (2013, 2015) combined a 1D radiative-convective model with a photochemical model to assess the effect of the spectral energy distribution of incident stellar spectra on atmospheric profiles, and observed an enhanced water mixing ratio in the stratosphere for planets around late-type stars. This was attributed to the higher surface temperatures and photochemical production from CH_4 which can more easily accumulate under M-star incident spectra.

Inevitably, 1D models rely on several assumptions that cannot be treated within the model, including the global transport of heat and water vapor, as well as the effect of clouds. Various three-dimensional (3D) general circulation models (GCMs) revisited the atmospheric structure of terrestrial planets and have demonstrated the importance of accounting for the 3D circulation and climate heterogeneity (e.g. Ishiwatari et al. 2002; Abe et al. 2011; Leconte et al. 2013a,b; Wolf & Toon 2014, 2015). Among others, Yang et al. (2013) pointed out that for synchronously rotating planets, the convection around the substellar point produces optically thick clouds which increase the planetary albedo and contribute to keep the surface temperature moderate for a much wider range of instellation (see also Yang et al. 2014; Way et al. 2015; Kopparapu et al. 2016). This situation is of particular relevance to the planets in the habitable zones of late-type stars as they are likely to be synchronously rotating due to tidal locking (Dole 1964; Kasting et al. 1993), although this need not always occur (Goldreich & Peale 1966; Leconte et al. 2015). They primarily studied the highest instellation that allows for the model to converge as a proxy for the inner edge. While they also presented the stratospheric water vapor amounts, the discussion was limited.

Motivated by these works on the stabilized climate of synchronously rotating planets, we are specifically interested in the water vapor transport into the upper atmosphere, not only because it affects the water loss rate (and thus the conventional criterion for habitable conditions) but also because it limits our ability to detect H_2O signatures of planets with surface liquid water, through transmission spectroscopy. Indeed, planets around later type stars, which are more likely to be synchronously rotating, are best suited for future transit observations for several reasons, including the higher transit probability, larger signals in transmission spectra, and the abundance of late-type stars in the nearby universe.

In order to obtain better insights into the processes that control the water vapor mixing ratio in the upper atmosphere of synchronously rotating terrestrial planets with surface water, we conduct a series of experiments using the ROCKE-3D GCM, which calculates the atmospheric dynamic, thermodynamic, and radiative fields up to 0.1 mbar (~65 km in the case of the Earth), sufficiently resolving the stratosphere. We specifically study the dependence of the water vapor mixing ratio on the incident flux (total incident flux and the spectral type), fixing planetary parameters (radius, gravity, atmospheric composition, and atmospheric pressure). We also present synthetic transmission spectra based on GCM outputs in order to evaluate the detectability of H_2O signatures with future transmission spectroscopy.

The organization of this paper is as follows: Section 2 describes the set-up of our GCM experiments and calculations of transmission spectra. Section 3 discusses our results of water vapor profiles as a function of the incident spectrum, and shows the modeled transmission spectra. The sensitivities of our results to the ocean model, the CO_2 abundance, and the spin period are studied in Section 4. Finally, Section 5 summarizes our findings.

2. MODEL

2.1. *GCM experiments*

We use the ROCKE-3D GCM (Way et al. 2017) to obtain 3D atmospheric structures of planets with varying total incident flux and spectral type of the star, focusing on the H_2O profile in the upper atmosphere. ROCKE-3D is a generalization of the ModelE2 GCM (Schmidt et al. 2014), which has been developed for the Earth at NASA's Goddard Institute for Space Studies. The details of the ROCKE-3D GCM are presented in Way et al. (2017).

In the following, we first describe the specific configurations in our experiments to clarify our targets. Then, we also discuss in some detail the convection/cloud parameterizations and the radiation parameterization used in our GCM, as these are of particular importance to our results.

2.1.1. *Our Configurations*

Throughout the paper, we exclusively consider synchronously rotating planets due to their relevance to fu-

TABLE 1
Stellar Properties

Star	Type	$T_{\rm eff}$	L [$L_\odot$]	M [$M_\odot$]	R [$R_\odot$]	reference	source of spectrum
Sun	G2V	5772 K	1	1	1	-	Lean et al. (2005), SPARC/SOLARIS[a]
HD 22049	K2V	5039 K	0.32	0.82	0.74	Baines & Armstrong (2012)	Segura et al. (2003)
Kepler 186	M1V	3755 K	0.055	0.544	0.523	Torres et al. (2015)	Allard et al. (2012)
GJ 876	M4V	3129 K	0.0122	0.37	0.3761	von Braun et al. (2014)	Domagal-Goldman et al. (2014)

[a] http://solarisheppa.geomar.de/ccmi

ture transmission observations of close-in systems as discussed in Section 1.

We also only consider aquaplanets, i.e., planets whose surfaces are wholly covered with water. We use a thermodynamic ocean with 50 m depth for the fiducial runs for simplicity. However, in Section 4.1, we also present the results of runs with a fully dynamic ocean, to show that our conclusions are not very sensitive to ocean heat transport.

Our atmosphere has a mean surface pressure of 1 bar, and is composed mainly of N_2, with only 1 ppm CO_2, as in Kopparapu et al. (2016). In Section 4.2, we will briefly discuss the dependence of our results on the mixing ratio of CO_2. We did not include the effects of aerosols and photochemistry.

The model was configured to have a horizontal grid with 4 degree resolution in latitude and 5 degree resolution in longitude, and 40 vertical layers covering up to 0.14 mbar (corresponding to $\sim$ 65 km in the case of the Earth).

In our experiments, we mainly changed two parameters: the total incident flux and the spectral type of the star. For the latter, four types of stars are considered: Sun (G2V), HD 22049 (K2V), Kepler-186 (M1V), and GJ 876 (M4V). The spectra of HD 22049 and GJ 876 are obtained from Segura et al. (2003) and Domagal-Goldman et al. (2014), respectively, while the spectrum of Kepler-186 is a modeled spectrum from BT-Settl (Allard et al. 2012) based on the stellar parameters reported in Table S1 of Quintana et al. (2014). The physical parameters of these stars as well as the references are summarized in Table 1, and the spectra are displayed in Figure 1.

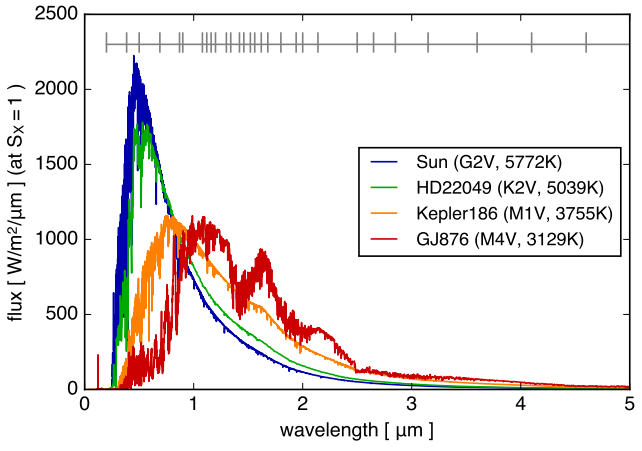

Fig. 1.— The spectra of the stars considered in this paper. The flux is normalized so that the total incident flux matches the solar constant. The data sources are listed in the right-most column of Table 1. The resolution of the spectra was lowered from the original data just for display purposes. The bands used by the short-wave radiation scheme in the GCM are indicated by the short grey vertical lines.

The orbital period (identical to the spin period) is changed according to Kepler's 3rd law, to be consistent with the total incident flux the planet receives and the stellar mass. Thus, the incident flux and the spin period are changed simultaneously for the fiducial set of runs. However, we also isolate the effect of the spin period in Section 4.3.

Our fiducial models with a thermodynamic ocean typically equilibrate in $\sim$ 30 Earth years in model time. After the steady state is reached, we average the 3D atmospheric profiles over an integer number of orbits that is approximately equal to 10 Earth years. All of the results presented in this paper are based on the averaged data created this way.

2.1.2. *Cloud Scheme*

Convection is triggered when a parcel lifted one model layer becomes buoyant according to a virtual moist static energy test. The cumulus parameterization uses a mass flux closure determined by the mass required to establish neutral buoyancy at cloud base over a specified adjustment time. The total mass flux is divided into two components ("plumes") that entrain at different rates (Del Genio et al. 2007). The plume rises until the updraft speed decreases to zero. Entrainment is proportional to parcel buoyancy and inversely proportional to the square of updraft speed, following Gregory (2001). Mass is detrained at all levels above the level of neutral buoyancy. A downdraft forms at any level when an equal mixture of cloud and environment is negatively buoyant. Updraft convective condensate is partitioned into fractions that precipitate, detrain, and are carried upward by assuming a Marshall-Palmer particle size distribution and empirical size-fall speed relationships and calculating the fraction of the size distribution whose fall speed exceeds, is comparable to, or is less than the diagnosed updraft speed (Del Genio et al. 2005).

Detrained condensate is treated by the stratiform cloud microphysics (an updated version of Del Genio et al. 1996). Stratiform cloud fraction is diagnosed as a function of relative humidity and stability, while condensed water evolves using a prognostic equation that includes representation of all relevant microphysical source and sink processes. Partitioning between the liquid and ice phase is specified as a function of temperature in the mixed phase temperature range, and then modified by a parameterization of diffusional growth of ice when snow falls into a supercooled liquid water layer.

2.1.3. *Radiation Scheme*

For the radiation scheme, we adopt the Suite of Community RAdiative Transfer codes based on Edwards and Slingo[1] (SOCRATES, Edwards & Slingo 1996; Edwards 1996) as described in Way et al. (2017). This radiation scheme uses the two-stream approximation of Zdunkowski & Korb (1985) with a diffusivity of $D = 1.66$ for the long-wave (thermal) component, and of Zdunkowski et al. (1980) with $D = 2$ for the short-wave (stellar) component. Opacities are treated using the correlated-k method (Lacis & Oinas 1991; Goody et al. 1989), with k-terms derived using exponential sum fitting of transmissions (Wiscombe & Evans 1977) based on HITRAN2012 (Rothman et al. 2013). H_2O continuum absorption is treated using the CAVIAR continuum (Ptashnik et al. 2011). Overlapping gaseous absorption is treated using equivalent extinction (Edwards 1996; Amundsen et al. 2017).

The optical properties of liquid clouds were derived using Mie theory, with the effective radius diagnosed from the cloud water content assuming a specified number concentration for liquid clouds. The optical properties of ice crystals are described in Edwards et al. (2007), and are based on the representation of ice aggregates introduced by Baran et al. (2001), with the effective dimension calculated using a parametrization based on temperature. Convective and stratiform clouds are treated separately, and if both are present in the same grid box they are treated as randomly overlapping to calculate the total cloud fraction within the grid box. Vertical cloud overlap is treated using the maximum-random overlap assumption, where clouds in adjacent layers overlap maximally, while clouds separated by one or more layers overlap randomly.

The configuration of the long-wave radiation scheme adopted here is the same as that used by the UK Met Office for global atmosphere configuration 7.0 (GA7.0; Walters et al. 2017). For short-wave radiation, we use 29 bands, as indicated by the grey vertical lines in Figure 1 and listed in Table 2, in order to ensure accuracy of the short-wave absorption. The wavelengths are weighted internally in each band by each stellar spectrum when deriving k-coefficients and cloud optical properties to further improve accuracy. We check the accuracy of the short-wave radiation scheme by comparing the flux and heating rate obtained with 29 bands to higher-resolution calculations, and find a good match; see Appendix A for more details.

2.2. *Simulation of transmission spectra*

We also simulate transmission spectra based on the outputs of our GCM experiments, setting the modeled planet in a transiting geometry, in order to quantify the absorption features of water vapor. We follow the procedure described in Appendix B of Way et al. (2017), which is briefly summarized below.

First, we obtained the vertical profiles of temperature, water vapor, and cloud particles along the terminator (i.e., dayside-nightside boundary) by linearly interpolating the profiles of the GCM gridpoints adjacent to the terminator. Then, we trace the optical paths of the transmitted ray according to the profile of the refraction index, from the observer toward the stellar disk, in the same way as described in van der Werf (2008), following Misra et al. (2014). After that, the spectral opacity at different points along the path is calculated considering Rayleigh scattering, the absorption by atmospheric molecules, and absorption and scattering by cloud particles, excluding the effects of multiple scattering. The spectral signatures of the planetary atmosphere are discussed in terms of the transit depth $\Delta F(\lambda)$ where λ is the wavelength, as well as the effective height, $h_{\rm eff}$, which is given as a function of planet radius, $R_{\rm p}$, and stellar radius, $R_\star$, by

$$\Delta F(\lambda) = \frac{(R_{\rm p} + h_{\rm eff}(\lambda))^2}{R_\star^2}. \quad (1)$$

To compute the absorption coefficients of atmospheric molecules, we use line-by-line opacity tables based on the HITRAN2012 database (Rothman et al. 2013), prepared separately from the opacities used in the GCM.

Including the optical effects of clouds is tricky. Strictly speaking, one needs to know the size distribution and the spatial distribution of the cloud particles at the time scale of the planetary transit. In this paper, when calculating transmission spectra, we consider the effect of clouds only in an approximate manner with four assumptions: Firstly, we assume that the radius of the cloud particles $r_{\rm cld}$ is $r_{\rm cld} = 30$ μm (regardless of their phase), similar to the typical values of ice cloud particles on the Earth as well as in our GCM simulations. Secondly, that the scattering cross section is given by that of the geometric optics limit, i.e. $2\pi r_{\rm cld}^2$. Thirdly, that cloud particles are uniformly distributed within each grid cell. Fourthly, we compute the transmitted light based on the optical properties averaged over 10 Earth years, rather than computing it based on the instantaneous optical properties before taking the temporal average. The third and fourth points above imply that the effects of clouds we find are the largest among the possible realizations given the particle size distribution, because of the non-linear dependence of transmittance on the optical thickness. Under these assumptions, the absorption coefficient k of the clouds is

$$k = 2\pi r_{\rm cld}^2 \cdot n = 3\rho x_{\rm cld}/(2\rho_{\rm H2O} r_{\rm cld}), \quad (2)$$

where n is the number density of cloud particles, ρ is the density of the ambient atmosphere, $x_{\rm cld}$ is the cloud water content provided by the GCM experiments, and $\rho_{\rm H2O}$ is the density of liquid/solid water, which is assumed to be $1{\rm g/cm}^3$. The uncertainties in the particle radius, scattering cross section, and the cloud water content could change the absorption coefficient by a factor of a few.

3. RESULTS

3.1. *General Trend in 3D Atmospheric Structures*

Before examining the dependence of the water vapor mixing ratio in the upper atmosphere, we discuss the 3D structures of temperature and water vapor as we need to know at which altitude the mixing ratio of water vapor becomes relatively uniform, in order to identify a suitable water vapor mixing ratio that can be regarded as representative of the humidity in the upper atmosphere.

[1] https://code.metoffice.gov.uk/trac/socrates

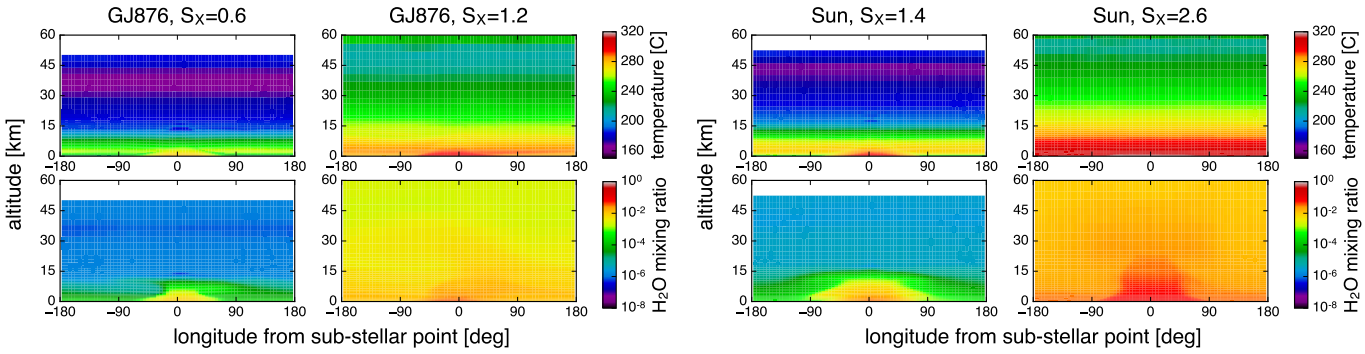

FIG. 2.— Profiles of temperature (upper panels) and water vapor mixing ratio (lower panels) along the equator, for GJ 876 (a M4V star; left) and for Sun (right), with different total normalized incident flux (S_X). The blank area near the top is above the model top (< 0.14 mbar).

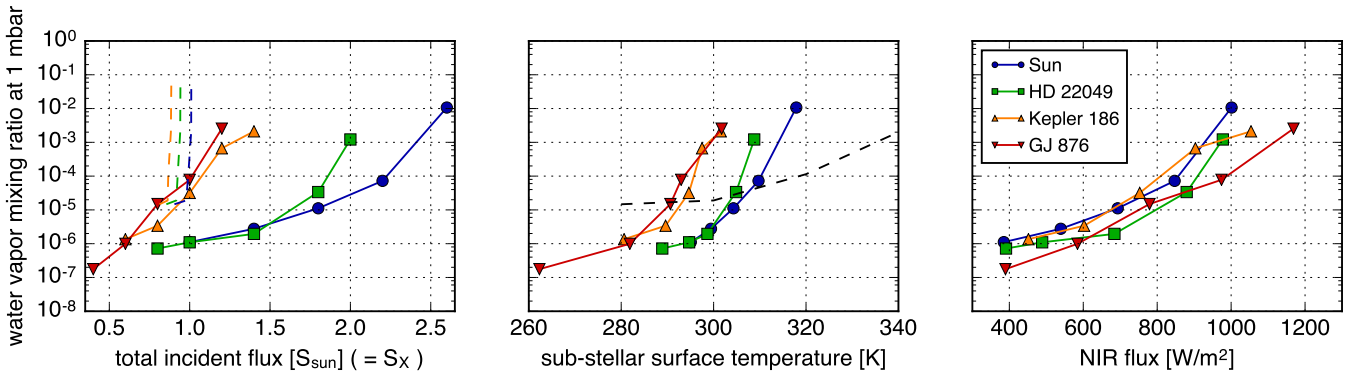

FIG. 3.— Water vapor mixing ratio at 1.39 mbar (x_{H_2O}) as a function of total incident flux (left), the surface temperature averaged within $0.2R_\oplus$ of the substellar point (center), and the near-infrared portion of the incident flux integrated between 0.9 and 3.0 μm (right). The colors represent the stellar types: Sun (navy), HD 22048 (green), Kepler-186 (orange), and GJ 876 (red). Dashed lines in the left panel are adapted from the 1D model of Kopparapu et al. (2013) for varying stellar effective temperatures: 5800 K (navy), 4800 K (green), and 3800 K (orange). The dashed black line in the middle panel is also adapted from Kopparapu et al. (2013).

Figure 2 shows the structures of temperature and water vapor mixing ratio along the equator for the planets around GJ 876 (M4V) and around the Sun (G2V), respectively, for varying incident flux normalized by the solar constant (S_X). In all panels the substellar point corresponds to 0° longitude. In general, the temperature and the water vapor mixing ratio near the surface strongly depend on the distance from the substellar point, but are fairly uniform in the upper part of the atmosphere. Above 1 mbar, which is located between 35 and 50 km altitude depending on the atmospheric temperature profiles, the water vapor mixing ratio becomes horizontally uniform within a few tens of percent. Therefore, in the following, we denote the globally averaged water vapor mixing ratio at 1.39 mbar by x_{H_2O}, and use it as representative of the water vapor abundance in the upper atmosphere.

We also observe optically thick clouds around the substellar point and a resulting increase of the planetary albedo as a function of total incident flux (not shown in figures), consistent with Yang et al. (2013, 2014), Kopparapu et al. (2016) and Way et al. (2016). As shown in Figure 2, the maximum surface temperature does not exceed 320 K even in the highly irradiated cases in our experiments where the water vapor mixing ratio near the model top is as high as 10^{-3}; we will discuss this in the subsequent sections.

3.2. *Response of Water Vapor Mixing Ratio to Increased Incident Flux*

In this section, we examine in more detail how the water vapor mixing ratio in the upper atmosphere depends on the incident flux (both the total flux and the spectral distribution).

The left panel of Figure 3 presents x_{H_2O} versus S_X. Overall, we find an increase of x_{H_2O} as a function of S_X. However, the slope is much more gradual than suggested by 1D models, in particular those of Kasting et al. (1993) and Wordsworth & Pierrehumbert (2013) with a small CO_2 mixing ratio, which typically predict a rapid transition from an Earth-like dry stratosphere to a H_2O-dominated atmosphere. Our result that the water vapor mixing ratio responds more slowly to the incident flux is qualitatively consistent with Yang et al. (2013), who studied synchronously rotating planets using CAM3 with an emphasis on the stability of the climate. Note that we cannot directly compare to their results as our assumptions do not match perfectly; specifically, Yang et al. (2013) assumed a planet with larger radius ($R = 2R_\oplus$) and higher gravity ($g = 1.4g_\oplus$), and a 60-day orbital period. The dependence on these other planetary parameters will be investigated in a future paper.

Because these are synchronously rotating planets where the surface temperature is stabilized by the opti-

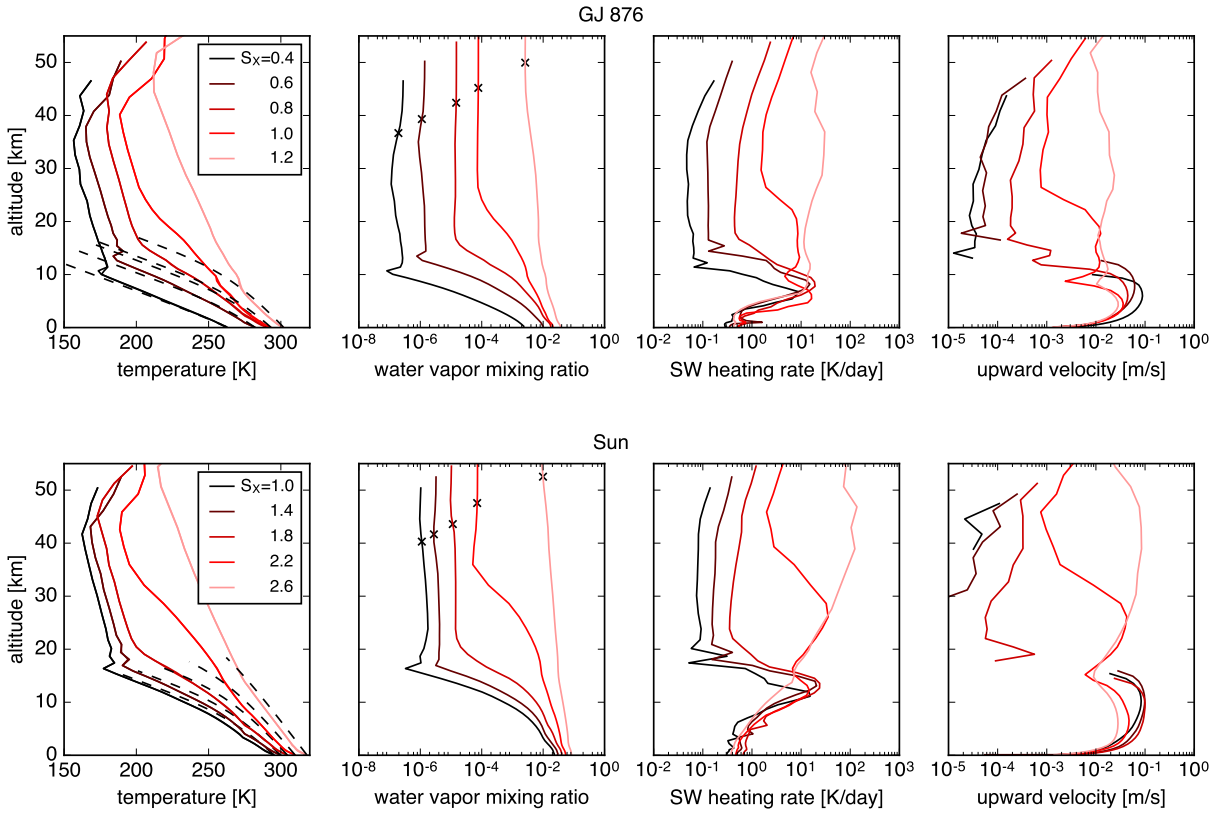

FIG. 4.— From left to right, the vertical profiles of temperature, water vapor mixing ratio, short-wave heating rate, and upward velocity, averaged within $0.2R_\oplus$ of the substellar point, for a planet around GJ 876 (top) and around the Sun (bottom) with varying total incident flux. Dashed lines in the left-most panels show the moist adiabat drawn from the same surface temperature. The cross marks indicate the altitude of 1.39 mbar where $x_{\mathrm{H_2O}}$ is measured. In the right-most panel, the altitudes with negative upward velocity are not shown.

cally thick clouds around the substellar point, one might think that this stabilized surface temperature would explain the slow response of water vapor to the increased total incident flux. To see the effect of the surface temperature, we have plotted $x_{\mathrm{H_2O}}$ as a function of surface temperature around the substellar point, where convection is strongest (Figure 3, middle panel). It is then clearly seen that the water vapor mixing ratio starts to rise at a fairly modest surface temperature and increases even more dramatically as a function of surface temperature than 1D models suggest. This indicates that the increasing surface temperature cannot by itself explain the increased stratospheric water vapor mixing ratios.

Instead, we find that the NIR component of the incident flux appears to be a good predictor of stratospheric humidity across the full range of stellar spectral types (Figure 3, the right panel). Here, we integrated the star spectra between 0.9 and 3 μm (the interval is somewhat arbitrary) to obtain the NIR component of the incident flux. We will examine the reason for this in the next subsection.

3.3. *Development of Large-Scale Circulation in the Upper Atmosphere*

In Figure 4, we show the vertical profiles of temperature, water vapor mixing ratio, short-wave heating rate, and upward velocity, averaged over the region within a distance $0.2R_\oplus$ from the substellar point. The variability of the profiles in the individual gridboxes that contribute to the average is negligible compared to the changes due to varying S_X. Rising motion exists at most altitudes in the substellar region. In the troposphere, where moist convection occurs, large-scale vertical motion is relatively insensitive to S_X. Above the convective layers, though, large-scale upward motion increases strongly with incident flux, concurrently with the increase in water vapor mixing ratio and heating rate in the upper atmosphere.

Here in the upper atmosphere we see the interplay among the radiative heating, water abundance, and the vertical air transport: When the incident flux increases, the radiative heating due to the absorption of short-wave radiation by water vapor and potential cloud particles, mainly in the near-infrared (NIR) regime, also increases. The air then reacts by rising and adiabatically cooling. The induced upward motion of the atmosphere transports water vapor from the moist lower atmosphere to the upper atmosphere, lowering the vertical gradient of water vapor and increasing the moisture at high altitude, further increasing the short-wave heating.

To be more specific, the evolution of the profile satisfies the conservation equation for the potential temperature:

$$\frac{T}{\theta}\left(\frac{\partial\theta}{\partial t}+(\mathbf{v}\cdot\nabla)\,\theta\right)=\frac{Q_r+Q_l}{\rho c_p}, \tag{3}$$

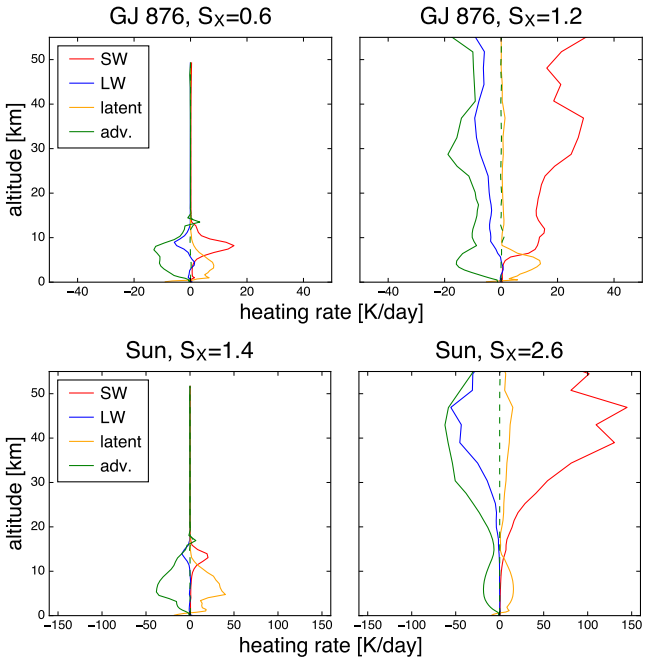

FIG. 5.— Contribution of different physical processes to the heating rate in the substellar regions in the cases of low (left) and high (right) irradiance, for GJ876 (top) and the Sun (bottom). Red: heating rate from short-wave radiation, blue: long-wave radiation, orange: latent heat, green solid: vertical advection, green dashed: horizontal advection.

or

$$\frac{T}{\theta}\frac{\partial\theta}{\partial t} = -\frac{T}{\theta}\left(u\frac{\partial\theta}{\partial x} + v\frac{\partial\theta}{\partial y}\right) - \frac{T}{\theta}\left(\omega\frac{\partial\theta}{\partial p}\right) + \frac{Q_r}{\rho c_p} + \frac{Q_l}{\rho c_p}, \quad (4)$$

where p is the pressure, Q_r and Q_l are the radiative and latent heating rates, c_p is the specific heat of the atmosphere at constant pressure, ρ is atmospheric density, $\{u, v, \omega\}$ are the conventional velocity components toward the east ($x-$axis), north ($y-$axis), and upward ($z-$axis; expressed here in pressure coordinates as $\omega \equiv dp/dt$), respectively. Given that the horizontal advection (the last term on the right-hand side) has a negligible contribution since the horizontal gradients are small (Figure 2), and that the latent heating (the first term on the right-hand side) is also negligible above the altitude to which convection penetrates, the increase of the radiative heating in the upper atmosphere must be compensated by the adiabatic cooling by vertical advection. The contribution of each term of the right-hand side of equation (4) in the steady state is shown in Figure 5, for the substellar regions of low and high irradiation cases with GJ876 and the Sun. It is clearly seen that the net radiative heating at high irradiation cases is compensated by the cooling by the vertical advection.

Figure 6 puts this upward motion in the sub-stellar regions into the global context, by presenting the velocity fields in the altitude-longitude plane along the equator for the low and high irradiation cases for GJ876 and the Sun. Here, the vertical components of the vectors are multiplied by 1000 to make them more visible, because large-scale vertical motions are about three orders of magnitude weaker than horizontal motions. The development of the large-scale circulation above the troposphere is clearly seen.

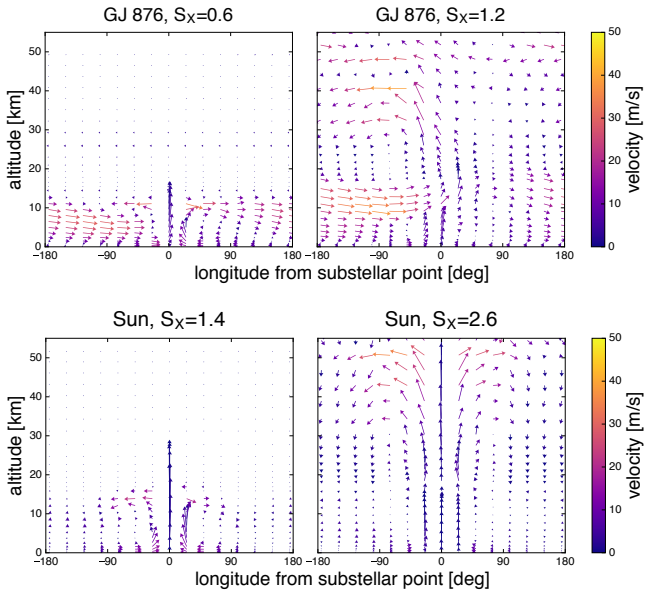

FIG. 6.— Velocity fields along the equator in the cases of low (left) and high (right)irradiance, for GJ876 (top) and the Sun (bottom). The vertical components of the vectors are multiplied by 1000 for display purposes, while the colors show the absolute values, $\sqrt{v_x^2 + v_z^2} \sim v_x$.

Altogether, Figures 4, 5 and 6 suggest that the stratospheric dynamical response to increased stellar radiation is similar for stars of different spectral type, but for a warmer star the onset of strong upward motion occurs at a much larger incident flux because less of the instellation is in NIR where the radiation is more efficiently absorbed by water vapor and clouds. This is the reason for the behavior seen in the right panel of Figure 3.

We also note that the contribution of radiative heating by cloud particles above convective layers is not negligible. In order to see the radiative effect of clouds above convective layers, we created models that are comparable to the fiducial models, but where the influence of cloud particles above the 237 mbar level ($\sim$ 11 km for the runs shown below) has been turned off in the radiation calculations (i.e., clouds particles in the upper atmosphere are transparent to radiation). Figure 7 displays the comparison between such "transparent high clouds" models (black, dotted) and fiducial models (red solid), for $S_X = 1.0$ and 1.2 with the incident spectrum of GJ 876. While these high clouds have a minimal effect on the surface temperature and atmospheric profiles below the convection layers, it is seen that radiative heating above the convection layer is substantially suppressed without the radiative effect of clouds, leading to a colder, and drier upper atmosphere. Note that we still see heating attributed to water vapor in the "transparent high clouds" models, for example, the water vapor mixing ratio and short-wave heating at 20-30 km altitude increase considerably from $S_X = 1.0$ to $S_X = 1.2$ even in the absence of cloud radiative effects, but the sensitivity to S_X is weaker at higher altitudes. We also ran equivalent simulations for other types of stars and found that the overall effects of the "transparent high clouds" assumption are very similar.

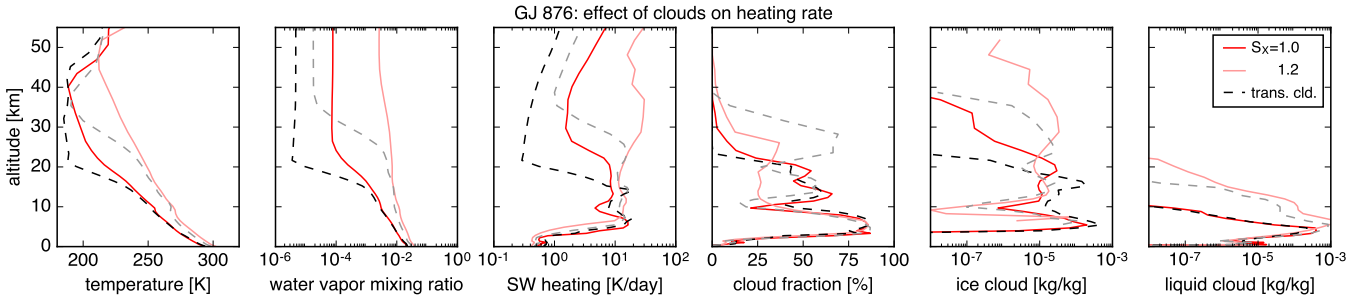

FIG. 7.— Comparison between the fiducial $S_X = 1.0$ (red) and $S_X = 1.2$ (pink) models of of planets orbiting GJ 876 and the comparable "transparent high clouds" models where the radiative effect of high clouds above 237 mbar are turned off (dashed black for $S_X = 1.0$ and dashed gray for $S_X = 1.2$). The vertical profiles of temperature, water vapor mixing ratio, short-wave heating rate, cloud fraction, ice cloud content, and liquid cloud content are averaged over the region within $0.2R_\oplus$ of the substellar point.

In summary, atmospheric vertical motion and the radiative heating by water vapor and cloud particles interact with each other through positive feedbacks, and thus a modest increase of the incident radiative flux, S_X, can result in an order-of-magnitude or more increase of the water vapor mixing ratio in the upper atmosphere, while the surface temperature increases only modestly due to the stabilization by clouds. This picture is verified by a good correlation between the water vapor mixing ratio at 1.39 mbar and the NIR portion of the incident flux as shown in the right panel of Figure 3, insensitive to the stellar spectral types. Because the NIR flux is an external parameter that can be found from direct observations of the host star, it would be a useful guide to predict the high-altitude water vapor mixing ratio for a planet with surface liquid water given knowledge of its distance from the star.

3.4. *Transmission Spectra*

In this subsection, we show the dependence of the transmission spectra on the incident flux, taking the modeled planets around one of our M-type stars, GJ 876 as examples. Figure 8 shows the transmission spectra for the $S_X = 0.6$, 1.0 and 1.2 cases, where the water vapor mixing ratio at 1.39 mbar is roughly 10^{-6}, 10^{-4} and $3 \cdot 10^{-3}$, respectively. The corresponding vertical profiles in the substellar region are shown in Figure 4, and note that the water vapor mixing ratio is even higher at medium altitudes (10 to 30 km). Although refraction due to the planetary atmosphere is included, its effect on the transmission spectra of planets around late-type stars like GJ 876 is minor (Bétrémieux & Kaltenegger 2014; Misra et al. 2014).

Without the opacity due to clouds (colored dashed lines in Figure 8), the effective altitude of the water vapor absorption features increases from ∼15 km to ∼40 km when S_X increases from 0.6 to 1.2. This level of effective altitude of water signatures is comparable with the strongest features (CO_2) in the modeled visible-to-NIR transmission spectrum of the Earth (solid black line) , and substantially larger than the H_2O signatures of the Earth. Note that the feature around 2.7μm is the overlap between H_2O and CO_2, and in our simulation cases with 1 ppm of CO_2 the feature predominantly comes from H_2O, while in the case of the Earth it mostly comes from CO_2. Thus, for the highly-irradiated cases shown here, H_2O signatures will be a natural target when trying to observe the strongest atmospheric signatures of planets similar to the Earth.

However, we also find clouds in the upper atmosphere around the terminator, and the inclusion of clouds substantially raises the baseline of the transmission spectra. (Note that the high clouds discussed in the previous sections are those around the substellar point, while what matter here for the transmission spectra are those at the terminator.) These clouds at the terminator presumably form from water vapor that is transported from the substellar point and cools radiatively or adiabatically. Although these tenuous clouds at high altitude would be optically thin vertically, the grazing geometry of transmission observations cause them to significantly affect the transmission spectra due to the long optical path length. After including the effect of clouds, however, we still find the overall increase of water vapor signatures as the incident flux increases. Compared to the standard Earth model, or the low-irradiation case (water vapor mixing ratio $\sim 10^{-6}$) with the same assumptions for the cloud optical properties, the signal of a high-irradiation case could be larger by a factor of a few.

For idealized cases, where the only source of obser-

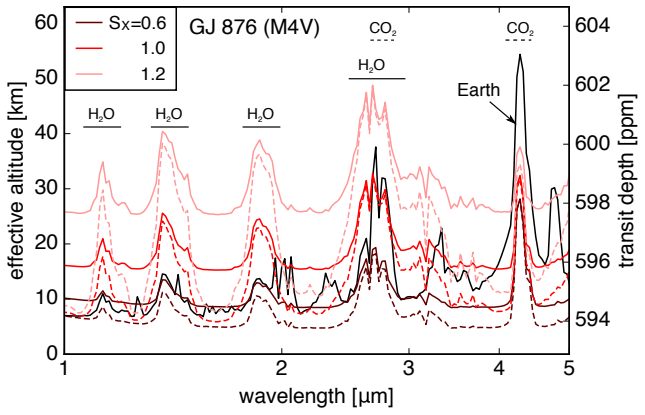

FIG. 8.— Modeled transmission spectra based on GCM experiments for planets around GJ 876 (M4V) with $S_X = 0.6$ (dark red), 1.0 (red) and 1.2 (pink), with (solid) and without (dashed) clouds. The corresponding vertical profiles in the substellar region are shown in Figure 4. The left-hand side of the y-axis shows the effective altitude, while the right-hand side indicates the transit depth in ppm using the size of the star from Table 1. The spectral resolution is lowered to $\mathcal{R} = 100$. For a reference, the black solid line shows the modeled transmission spectrum of the Earth based on the US standard atmosphere.

vational uncertainty is photon noise, we can evaluate the detectability of these features. For an Earth-sized planet 10 pc away, assuming a 6.5 m telescope (having the James Webb Space Telescope in mind) with 40 % throughput and the wavelength resolution $\mathcal{R}$ =20, absorption features with 20 km differential effective altitude in this wavelength range (e.g., the feature around 2.7 μm for the cases with clouds) would become detectable (5σ) after $\sim$ 100 hours of integration with an M4 star (assuming blackbody radiation with $R_\star = 0.4R_\odot$, T=3500 K, similar to GJ 876), or after $\sim$ 15 hours with an M8 star (with $R_\star = 0.1R_\odot$, T=2500 K, similar to TRAPPIST-1 planets), respectively.

4. SENSITIVITY EXPERIMENTS

In this section we examine the sensitivity of our results to some of our assumptions. In particular, we discuss the effect of the assumption of a simple thermodynamic ocean, the effect of the background CO_2 mixing ratio, and the effect of the spin period.

4.1. *Effect of Ocean Model*

So far, we have used a thermodynamic ocean model with zero ocean heat transport and 50 m depth. Indeed, this simplified treatment has been regularly used in previous 3D atmospheric modeling studies of exoplanets. A more realistic approach is to include the dynamics of the ocean. Therefore, we check whether our results are sensitive to the prescription of the ocean by comparing our fiducial results and those obtained using a dynamic ocean module.

For this purpose, we ran the models for GJ 876 assuming a 900 m deep dynamic ocean. The models with the dynamic ocean typically equilibrated after a hundred to several hundred Earth years. In the same way as the fiducial models, we averaged the atmospheric profiles over approximately 10 Earth years after the model reached a steady state.

Figure 9 shows x_{H_2O} for GJ 876 with varying S_X both for our fiducial runs and those using the dynamic ocean module. There are minor differences between the two, with the maximum difference being less than an order of magnitude. The models with a dynamic ocean tend to have somewhat less x_{H_2O} than the models with zero ocean heat transport. This appears to be related to the fact that ocean heat transport from the dayside to the nightside lowers the substellar surface temperature and weakens convection there, and thus there is less transport of water vapor to the upper atmosphere.

Overall, however, our fiducial models with a thermodynamic ocean give a reasonable order-of-magnitude estimate of water vapor mixing ratio in the upper atmosphere.

4.2. *Effect of CO_2*

Our fiducial models assumed 1 ppm CO_2, which was an arbitrary choice. Although a full investigation of the dependence on the CO_2 mixing ratio is beyond the scope of this paper, here we briefly mention how much the results are changed if we assume an Earth-like CO_2 mixing ratio. The results of the models with 300 ppm of CO_2 are plotted in Figure 9. As shown, this level of variation of CO_2 has a very small effect on the water vapor profile.

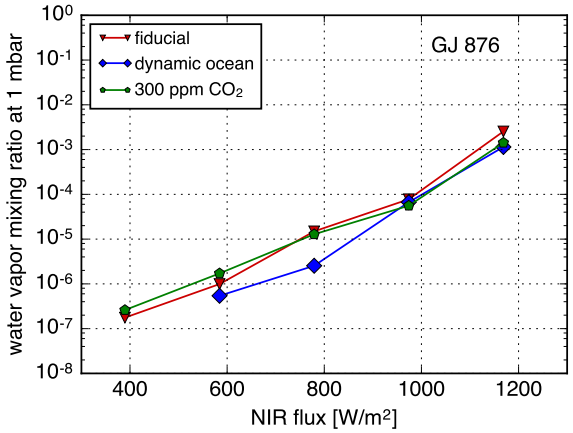

FIG. 9.— Water vapor mixing ratio at 1.39 mbar for the models using a dynamic ocean (blue diamonds) and the models with an Earth-like CO_2 mixing ratio (green pentagons), in comparison with the fiducial model with a thermodynamic ocean and 1 ppm CO_2 (red down-triangle).

Larger amounts of CO_2 up to that of a CO_2-dominated atmosphere could have a more substantial effect on the 3D profiles (Wordsworth & Pierrehumbert 2013).

4.3. *Effect of Spin Period*

In our fiducial set of experiments, we changed the planetary spin period together with the stellar flux for a given star, because we consider synchronously rotating planets and the orbital period (which is equal to the spin period) must change to be consistent with the total incident flux and the host star mass according to Kepler's 3rd law. Thus, strictly speaking, the change in the water vapor mixing ratio presented in Figure 3 includes the effect of both the varying incident flux and the varying spin period. Meanwhile, it is well known that the spin period has first order effects on the atmospheric circulation and hence can potentially affect x_{H_2O}.

In order to isolate the effects of rotation, we performed experiments where we varied the spin period while keeping the incident flux fixed at $S_X = 1$ with the GJ 876 spectrum, but allowing the planet to remain in synchronous rotation. The effect of varying spin period on x_{H_2O} is presented in Figure 10. It is considerably smaller than the dependence on S_X seen in Figure 3, i.e., the increase in stratospheric water vapor as the planet is moved closer to its star is mostly an intrinsic sensitivity to the stellar flux rather than an effect of the changing planet rotation as the orbital period changes.

The spin effect is non-negligible, however; we find that x_{H_2O} becomes smaller as the spin period gets very short, i.e., increasing planet spin partly offsets the effect of increasing stellar flux. Our interpretation of this tendency is as follows. At slow rotation (long spin period) the day-night circulation dominates the atmosphere. As the spin period becomes shorter, however, the atmosphere develops high-altitude zonal winds, as demonstrated in previous papers (Merlis & Schneider 2010; Edson et al. 2011; Kopparapu et al. 2016). The super-rotating zonal wind seen in the equatorial region in the shorter period runs (not shown) efficiently transports water vapor from the dayside to the nightside, limiting the cloudiness in the substellar region, and resulting in a higher surface

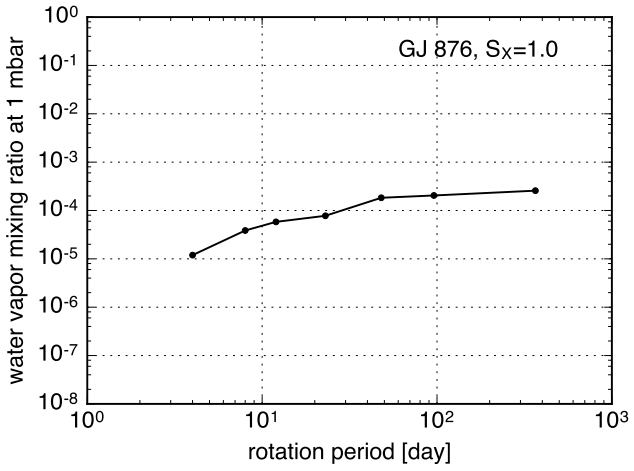

FIG. 10.— The dependence of water vapormixing ratio on the spin period. The host star spectrum is GJ 876 with $S_X = 1$. In all cases the planet is assumed to be synchronously rotating.

temperature (Kopparapu et al. 2016). Consistently, in the runs with a shorter spin period, the convection at the substellar point is deeper, and the temperature at the top of the convection where it moistens the atmosphere is colder, and thus the convection is less able to moisten the atmosphere there. Moreover, the water vapor transported upward by convection is more efficiently transported to the night side by the zonal wind, as noted above; the water vapor mixing ratio on the night side increases by about an order of magnitude when the rotation period decreases from 365 Earth days to 4 Earth days. These processes are likely to lead to the smaller upper atmosphere water vapor mixing ratio observed in our shorter shorter period runs.

5. SUMMARY

We have investigated the response of atmospheric water vapor profiles of synchronously rotating aquaplanets to changes in the incident stellar flux. We find a quasi-exponential increase of water vapor mixing ratios in the upper atmosphere as a function of total incident flux, resulting in a variation of several orders of magnitude as the total incident flux increases by a factor of two to three, but much more gradual than predicted by 1-D models.

The increase of water vapor mixing ratio in response to larger incident flux is not primarily caused by the increased surface temperature as previous 1D models suggest, due to the relatively stable surface temperature at the substellar point. Instead, it is induced by the effect of the increased NIR portion of the incident flux on the high-altitude circulation. The enhanced radiative heating due to the absorption by water vapor and cloud particles drives a large-scale circulation of the air at altitudes above those to which convection penetrates, taking over the role of transporting water vapor from the moist lower atmosphere to the upper atmosphere, and further increasing the heating rate in the upper atmosphere. As a result, the moisture in the upper atmosphere increases dramatically while the surface below it remains temperate. This picture is supported by the good correlation between the water vapor mixing ratio at 1.39 mbar and the NIR portion of the incident radiation, regardless of the spectral type of the host star.

Simulating transmission spectra based on the atmospheric profiles found in GCM experiments, we demonstrate that the increase of the water vapor mixing ratio at 1.39 mbar from 10^{-6} to 3×10^{-3} leads to an increase of the H_2O absorption depth by a factor of a few, making the effective altitude of the H_2O absorption features as high as 40 km. We also find the presence of high clouds at the terminator, which potentially increases the baseline effective altitude and thus weakens the absorption features. Our calculation may overestimate the effects of clouds on the transmission spectra due to the spatially and temporally averaged cloud properties of individual GCM grid cells. Additional uncertainties come from other assumptions we made. A more realistic inclusion of clouds in our simulated transmission spectra will be the scope of future work.

While we used a thermodynamic ocean model with zero ocean heat transport for simplicity, comparable experiments with a dynamic ocean are also performed to demonstrate that this approximation of an ocean has only a modest effect on the water vapor mixing ratio, the size of which is within about an order of magnitude or less. Varying the CO_2 mixing ratio from 1 ppm to 300 ppm has a negligible effect. We also confirmed that changing the planet spin period only has a secondary effect on the water vapor mixing ratio, resulting in an order of magnitude variation at most.

In this paper, we limit our discussion on the water vapor profiles to the effects of the total incident flux and spectral energy distribution (i.e., the spectral type of the host star). These parameters are among the limited number of properties that can be constrained relatively easily by observations. In principle, however, water vapor distributions also depend on geophysical parameters including the surface gravity, atmospheric composition, atmospheric pressure (e.g., Turbet et al. 2016), and the planetary water abundance, as well as photochemistry, which depends on the detailed atmospheric profiles. The dependence of the water vapor mixing ratio on these planetary properties will be the focus of future study.

We thank Michael J. Way and Nancy Y. Kiang for providing the boundary conditions for ROCKE-3D and for the helpful discussions. The support from Maxwell Kelley and Igor Aleinov was critical in resolving the issues identified in the process of generalizing ROCKE-3D for the exotic configurations considered in this paper. Y. F. is deeply grateful to David S. Spiegel for the insightful discussions on the simulation suite for transmission spectra. Y. F.'s research was supported by an appointment to the NASA Postdoctoral Program at the NASA Goddard Institute for Space Studies, administered by Universities Space Research Association under contract with NASA. We also acknowledge support from the NASA Astrobiology Program through the Nexus for Exoplanet System Science.

REFERENCES

Abe, Y., Abe-Ouchi, A., Sleep, N. H., & Zahnle, K. J. 2011, Astrobiology, 11, 443

Allard, F., Homeier, D., & Freytag, B. 2012, Philosophical Transactions of the Royal Society of London Series A, 370, 2765

Amundsen, D. S., Tremblin, P., Manners, J., Baraffe, I., & Mayne, N. J. 2017, A&A, 598, A97
Baines, E. K., & Armstrong, J. T. 2012, ApJ, 744, 138
Baran, A. J., Francis, P. N., Labonnote, L.-C., & Doutriaux-Boucher, M. 2001, Quarterly Journal of the Royal Meteorological Society, 127, 2395
Bétrémieux, Y., & Kaltenegger, L. 2013, ApJ, 772, L31
—. 2014, ApJ, 791, 7
Cowan, N. B., Greene, T., Angerhausen, D., et al. 2015, PASP, 127, 311
Del Genio, A. D., Kovari, W., Yao, M.-S., & Jonas, J. 2005, Journal of Climate, 18, 2376
Del Genio, A. D., Yao, M.-S., & Jonas, J. 2007, Geophys. Res. Lett., 34, L16703
Del Genio, A. D., Yao, M.-S., Kovari, W., & Lo, K. K.-W. 1996, Journal of Climate, 9, 270
Dole, S. H. 1964, Habitable planets for man
Domagal-Goldman, S. D., Segura, A., Claire, M. W., Robinson, T. D., & Meadows, V. S. 2014, ApJ, 792, 90
Edson, A., Lee, S., Bannon, P., Kasting, J. F., & Pollard, D. 2011, Icarus, 212, 1
Edwards, J. M. 1996, Journal of Atmospheric Sciences, 53, 1921
Edwards, J. M., Havemann, S., Thelen, J.-C., & Baran, A. J. 2007, Atmospheric Research, 83, 19
Edwards, J. M., & Slingo, A. 1996, Quarterly Journal of the Royal Meteorological Society, 122, 689
Ehrenreich, D., Tinetti, G., Lecavelier Des Etangs, A., Vidal-Madjar, A., & Selsis, F. 2006, A&A, 448, 379
Goldreich, P., & Peale, S. 1966, AJ, 71, 425
Goody, R., West, R., Chen, L., & Crisp, D. 1989, J. Quant. Spec. Radiat. Transf., 42, 539
Gregory, D. 2001, Quarterly Journal of the Royal Meteorological Society, 127, 53
Ishiwatari, M., Takehiro, S.-I., Nakajima, K., & Hayashi, Y.-Y. 2002, Journal of Atmospheric Sciences, 59, 3223
Kaltenegger, L., & Traub, W. A. 2009, ApJ, 698, 519
Kasting, J. F., Whitmire, D. P., & Reynolds, R. T. 1993, Icarus, 101, 108
Kodama, T., Genda, H., Abe, Y., & Zahnle, K. J. 2015, ApJ, 812, 165
Kopparapu, R. k., Wolf, E. T., Haqq-Misra, J., et al. 2016, ApJ, 819, 84
Kopparapu, R. K., Ramirez, R., Kasting, J. F., et al. 2013, ApJ, 765, 131
Lacis, A. A., & Oinas, V. 1991, J. Geophys. Res., 96, 9027
Lean, J., Rottman, G., Harder, J., & Kopp, G. 2005, Sol. Phys., 230, 27
Leconte, J., Forget, F., Charnay, B., Wordsworth, R., & Pottier, A. 2013a, Nature, 504, 268
Leconte, J., Forget, F., Charnay, B., et al. 2013b, A&A, 554, A69
Leconte, J., Wu, H., Menou, K., & Murray, N. 2015, Science, 347, 632
Merlis, T. M., & Schneider, T. 2010, Journal of Advances in Modeling Earth Systems, 2, 13
Misra, A., Meadows, V., & Crisp, D. 2014, ApJ, 792, 61
Ptashnik, I. V., McPheat, R. A., Shine, K. P., Smith, K. M., & Williams, R. G. 2011, Journal of Geophysical Research (Atmospheres), 116, D16305
Quintana, E. V., Barclay, T., Raymond, S. N., et al. 2014, Science, 344, 277
Rauer, H., Gebauer, S., Paris, P. V., et al. 2011, A&A, 529, A8
Rothman, L. S., Gordon, I. E., Babikov, Y., et al. 2013, J. Quant. Spec. Radiat. Transf., 130, 4
Rugheimer, S., Kaltenegger, L., Segura, A., Linsky, J., & Mohanty, S. 2015, ApJ, 809, 57
Rugheimer, S., Kaltenegger, L., Zsom, A., Segura, A., & Sasselov, D. 2013, Astrobiology, 13, 251
Schmidt, G. A., Kelley, M., Nazarenko, L., et al. 2014, Journal of Advances in Modeling Earth Systems, 6, 141
Segura, A., Krelove, K., Kasting, J. F., et al. 2003, Astrobiology, 3, 689
Sing, D. K., Fortney, J. J., Nikolov, N., et al. 2016, Nature, 529, 59
Tinetti, G., Vidal-Madjar, A., Liang, M.-C., et al. 2007, Nature, 448, 169
Torres, G., Kipping, D. M., Fressin, F., et al. 2015, ApJ, 800, 99
Turbet, M., Leconte, J., Selsis, F., et al. 2016, A&A, 596, A112
van der Werf, S. Y. 2008, Appl. Opt., 47, 153
von Braun, K., Boyajian, T. S., van Belle, G. T., et al. 2014, MNRAS, 438, 2413
Walters, D., Brooks, M., Boutle, I., et al. 2017, Geosci. Model Dev., in prep.
Way, M. J., Del Genio, A. D., Kelley, M., Aleinov, I., & Clune, T. 2015, ArXiv e-prints, arXiv:1511.07283
Way, M. J., Del Genio, A. D., Kiang, N. Y., et al. 2016, ArXiv e-prints, arXiv:1608.00706
Way, M. J., Aleinov, I., Amundsen, D. S., et al. 2017, ArXiv e-prints, arXiv:1701.02360
Wiscombe, W. J., & Evans, J. W. 1977, Journal of Computational Physics, 24, 416
Wolf, E. T., & Toon, O. B. 2014, Geophys. Res. Lett., 41, 167
—. 2015, Journal of Geophysical Research (Atmospheres), 120, 5775
Wordsworth, R., & Pierrehumbert, R. 2014, ApJ, 785, L20
Wordsworth, R. D., & Pierrehumbert, R. T. 2013, ApJ, 778, 154
Yang, J., Boué, G., Fabrycky, D. C., & Abbot, D. S. 2014, ApJ, 787, L2
Yang, J., Cowan, N. B., & Abbot, D. S. 2013, ApJ, 771, L45
Zdunkowski, W. G., & Korb, G. J. 1985, Promet, 2/3, 26
Zdunkowski, W. G., Welch, R. M., & Korb, G. 1980, Beiträge zur Physik der Atmosphäre, 53, 147

APPENDIX

A. VALIDATION OF RADIATION SCHEME USED IN ROCKE-3D

In this paper we applied the ROCKE-3D GCM to planets around stars with different spectral types. In doing so, special caution is needed regarding the accuracy of the short-wave radiative transfer calculation, because the baseline model of ROCKE-3D was developed for the Earth, and the radiative transfer calculation was optimized for the solar spectrum. We therefore modified the bands used by the short-wave radiation calculation in SOCRATES in order to improve accuracy for low-mass stars while at the same time maintaining the accuracy for Sun-like stars. Our adopted short-wave bands in this study are given in Table 2.

In order to check the accuracy of the short-wave radiative transfer calculation used in the GCM, we compare it to a more accurate higher resolution (280 bands) calculation using the same atmospheric profile. We use the atmospheric profile at the substellar point of a planet around GJ 876 with $S_X = 1.2$ (see Figure 4), but without clouds. This profile was chosen because of its extremely high water vapor mixing ratio, which is very different from that of the Earth. Assuming this profile, we calculated short-wave radiative fluxes with 29 bands (used in the GCM) and with 280 bands, with both the Sun and GJ 876 as the incident spectra.

We show in Figure 11 the short-wave (stellar) downward fluxes, upward fluxes and heating rates we obtained. Differences between the 29 and 280 band configurations are small, < 5 W/m^2 for fluxes and < 0.5 K/day for heating rates except at pressures $\ll 1$ mbar, throughout the atmosphere. We therefore conclude that the radiation scheme adopted here is sufficiently accurate.

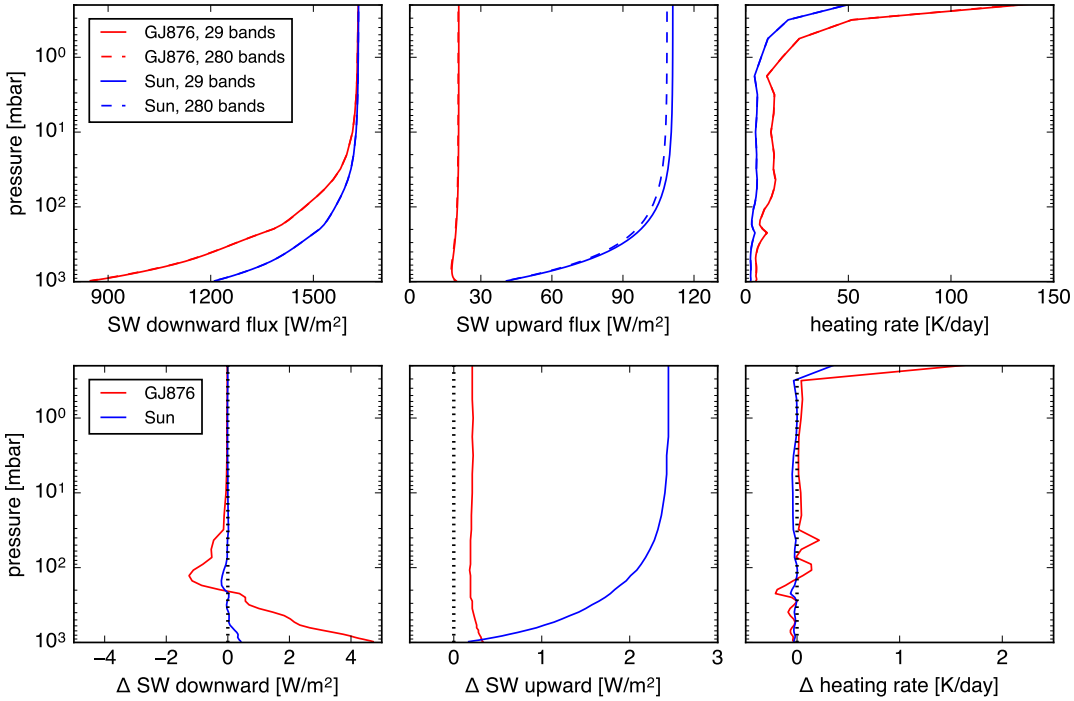

FIG. 11.— Comparison of shortwave downward fluxes (left), upward fluxes (center), and heating rates (left) between the 29 band shortwave radiative transfer used in the GCM and the 280 band benchmark. The atmospheric profile assumed is the one at the substellar point of a planet around GJ 876 with $S_X = 1.2$ (see the upper panels of Figure 4).

TABLE 2
THE SHORT-WAVE BANDS.

#	lower limit [mm]	upper limit [mm]
1	0.200	0.385
2	0.385	0.500
3	0.500	0.690
4	0.690	0.870
5	0.870	0.900
6	0.900	1.08
7	1.08	1.12
8	1.12	1.16
9	1.16	1.20
10	1.20	1.30
11	1.30	1.34
12	1.34	1.42
13	1.42	1.46
14	1.46	1.52
15	1.52	1.56
16	1.56	1.62
17	1.62	1.68
18	1.68	1.80
19	1.80	1.94
20	1.94	2.00
21	2.00	2.14
22	2.14	2.50
23	2.50	2.65
24	2.65	2.85
25	2.85	3.15
26	3.15	3.60
27	3.60	4.10
28	4.10	4.60
29	4.60	10.0